https://doi.org/10.1016/j.ijmecsci.2021.106359

Impact of initial fiber states on different fiber dynamic patterns in the laminar channel flow

Jingyu Cui[1], Yang Liu[1], Yuzhen Jin[2]

[1]Research Centre for Fluid-Structure Interactions, Department of Mechanical Engineering, The Hong Kong Polytechnic University, Hung Hom, Hong Kong, China

[2]Faculty of Mechanical Engineering & Automation, Zhejiang Sci-Tech University, Hangzhou, Zhejiang Province, China

Abstract

The dynamics of an elastic fiber with various initial states in a laminar channel flow is investigated using the immersed boundary-lattice Boltzmann method. Fiber-wall collisions are solved by adding a repulsive force in the model. Our simulation results demonstrate that the initial fiber state closely relates to the stability of the considered conveyance system. Different initial states may lead to different dynamic patterns in the downstream. The fiber is found to go straight forward along a horizontal path when it is horizontally and symmetrically placed at the channel centerline. Breaking this symmetry by varying the fiber's initial vertical position or orientation will induce the instability of the system, which then causes deviations and fluctuations in fiber's conveyance path. No matter how large the deviation occurs in the upstream, the fiber is always found to migrate to the channel central region in the downstream and would eventually settle in a vertical position slightly away from the channel centerline. Moreover, the off-centerline distance that a fiber settles depends on its dynamic pattern rather than a specific initial fiber state. For our system, there are two kinds of dynamic patterns observed in the downstream channel. In the first pattern, the fibers eventually reach their equilibrium states and are observed to do translational motions. In the second pattern, no equilibrium states are observable, and the fibers are found to do periodic tumbling motions. The fiber's eventual conveyance speed depends on the vertical position it eventually settles and can be roughly approximated by the local flow velocity.

Keywords: fiber dynamics, fiber conveyance, immersed boundary-lattice Boltzmann method, fluid–structure interaction

1. Introduction

The conveyance of fiber-like materials can be found in a variety of applications, for instance, in textile

manufacturing, biological system and composites processing. Among many of those applications, the fluid not only works as a delivery medium, but is also utilized to orientate fibers and maintain them in desired configurations. Take the rotor spinning as an example, straight fibers are more desirable in the yarn-formation process as it increases the tensile strength of the final spun yarn [1-3]. So buckled and folded fibers should be avoided or straightened during the fiber conveyance process. Besides the tensile strength, many other properties such as elastic modulus and thermal conductivity may depend on the configurations of fiber. Therefore, to satisfy certain properties of the fiber-related products, it is essential to accurately predict fiber dynamics during the conveyance through simulation, as it may provide insights for the optimal design of the conveyance system with respect to economics as well as quality.

Unlike the relatively well-studied dynamics of rigid fiber [4-6], the movement of a flexible fiber, however, is quite challenging to predict as it involves a complex fluid-flexible-structure interaction (FFSI). On one hand, the flow exerts drag forces on the fiber, forces it to move and simultaneously deforms its configuration. On the other hand, the fiber alters its ambient fluid motion due to the no-slip interface condition. When the flexibility is obvious, the fiber could present very complex dynamics, such as snake turns, “S” turns and complex coiling phenomena, as experimentally observed by Mason and his colleagues [7, 8]. This further gives rise to the complexity of modeling such a system, as the fluid-structure interface could be severely distorted, making it difficult to track the interface through a body-fitted grid.

Various fiber models have been proposed to simulate fiber dynamics. Yamamoto and Matsuoka [9, 10] modeled the fiber as a chain of spheres that are lined up and bonded to each neighbor (sphere model). This model can well reproduce the stretching, bending, and twisting behaviors of the fiber under hydrodynamic load. However, it is very computationally costly, as for each sphere, a translational and rotational equations need to be solved. Ross and Klingenberg [11] proposed a different fiber model, where flexible fibers are treated as linked rigid prolate spheroids connected through ball-and-socket joints (prolate spheroid model). Compared with the sphere model, the prolate spheroid model requires fewer rigid bodies to represent a fiber, thus takes less computation cost. There are other fiber models known as the needle-chain [12, 13] model and rod-chain model [14, 15], which share similar concepts by connecting a series of rigid segments through ball-and-socket joints to approximate fiber.

Apart from the above-mentioned fiber models that are dedicated to describing the fiber motion in shear flows, there are general FFSI frameworks exist for the modeling of thin elastic structures immersed in flows. One efficient framework is the slender body theory (SBT). The basic idea of SBT is to approximate the effect

of the obstacle (with a large aspect ratio) on its surrounding flow field by a distribution of singularities, whose strength is dependent on the imposed boundary conditions. Goldstein et al. [16] used a local SBT to study the intrinsic dynamics of a twisted elastic filament in a viscous fluid. Becker and Shelley [17] used a similar local drag model to investigate the shear-flow-induced deformation of a high-aspect-ratio elastic filament. The local SBT formulates the fluid-fiber interaction in a relatively simple manner (it gives a local anisotropic relation between elastic and drag forces). It cannot include the nonlocal interactions that mediated via the intervening fluid. To account for these interactions, different nonlocal versions of SBT were developed and exploited to study fiber/filament dynamics, for example in [18-22].

Another frequently used framework to study this class of problem is the immersed boundary method (IBM). The IBM is originally developed by Peskin to simulate blood flow through a heart valve [23-25]. Since its conception 1970s, it has found a wide variety of applications in moving/elastic boundary problems. One of the very first studies applying the IBM to simulate fiber dynamics can be found in the research of Stockie and Green [26], where the suspension of a massless (or neutrally buoyant) fiber in a two-dimensional shear flow was investigated at a moderate Reynolds number (*Re*). In their study, the experimentally observed "orbit classes" of fiber were well reproduced by tuning the fiber flexibility. Zhu and Peskin [27] used the IBM to simulate the laboratory observed flapping-filament problem. They found that the mass and length of the filament play a significant role in determining its final states. A massless filament is unable to sustain its flapping motion because it cannot exchange energy with the surrounding fluid. Huang et al. [28] proposed a different coupling strategy for this flapping-filament problem based on a feedback-forcing IBM. They studied the effect of fiber length and fixed-end boundary conditions on the bistability of the system. Their study also included the interaction between two side-by-side filaments. The flapping-filament problem was also studied by Tian et al. [29] with a modified penalty IBM, by Yuan et al. [30] with a momentum-exchange IBM, and by Goza and Colonius [31] using a strongly-coupled IBM. Apart from the flapping-filament problem, the IBM was also successfully used to simulate the conveyance of fiber in a trapezoidal channel [32], the falling motion of an inhomogeneous flexible filament [33], the migration of multiple fibers in blood stream [34], and the buckling and recuperation dynamics of diatom chain in a shear flow [35].

There are also many other FSI frameworks developed to study the dynamics of elastic thin structures (e.g fiber, filament, and two-dimensional flag). Pei and Yu [36] applied an arbitrary Lagrangian–Eulerian method to simulate the fiber motion in a nozzle of Murata vortex spinning. Connell & Yue [37] developed a coupled fluid–structure direct simulation (FSDS) method to investigate the flapping stability and response of a thin

two-dimensional flag. Alben [38] proposed a flexible body vortex sheet model to study the heaving and pitching motion of a slender elastic filament in high-*Re* flows.

It is now generally acknowledged that in the fluid-fiber interaction system, some parameters such as the flow *Re*, the fluid-fiber density ratio, the bending rigidity and length of the fiber, could play an important role in determining the fiber dynamics in a fluid flow. However, what is the role of the initial fiber state in a fiber conveyance/migration system? Does it have a significant impact on fiber dynamics, especially in the far downstream? and how? These are still open questions. As an attempt to seek answers for these questions, we performed a numerical study on the dynamics of a flexible fiber that conveyed in a laminar channel using the immersed boundary-lattice Boltzmann method (IB-LBM). As will be demonstrated in this paper, our numerical result suggests that the initial fiber state is closely related to the stability of the conveyance system. For the wall-bounded conveyance system we considered, both the fiber's initial vertical position and orientation are found to have a great impact on the fiber's dynamic pattern, equilibrium state, and conveyance efficiency.

2. Physical model

A schematic view of our considered problem is given in Fig. 1. In our current study, we assume that the fiber moves only in the x-y plane and has no out-of-plane motions due to the symmetry of the conveyance system in the z-direction and the laminar flow regime considered. Under these assumptions and as an initial step, our simulations are performed in two-dimensional. Apart from that, some previous studies [35, 39] have already demonstrated that two-dimensional simulations can also bring reasonable results for filament-like structure immersed in a laminar flow with a regular geometry. The computational domain, as shown in Fig.1, is a two-dimensional long rectangular channel with two open ends and two sidewalls to confine the flow. To make the wall effect obvious, the distance of the two sidewalls D is set as three times the undeformed length of fiber L_f (i.e. $D = 3L_f$, which is a typical width of the fiber transport channel of a rotor spinning machine). A viscous airflow with a parabolic velocity profile comes from the channel inlet in the x-direction to convey an elastic fiber. The fiber's midpoint initially locates at (L_f, H_0^*) and its initial end-to-end orientation angle is θ_0 with respect to the horizontal ($H_0^* = y_0/D$ is the initial vertical position, where y_0 is the initial y-coordinate of the middle point, and -90°$\leq \theta_0 \leq$90°, where $\theta_0 = 0°$ and $\theta_0 = \pm 90°$ correspond to horizontal and vertical orientations, respectively). It should be noted that for all the simulation cases the unstressed state of the fiber is assumed intrinsically straight and the fiber is released at a zero velocity when the flow gets fully

developed.

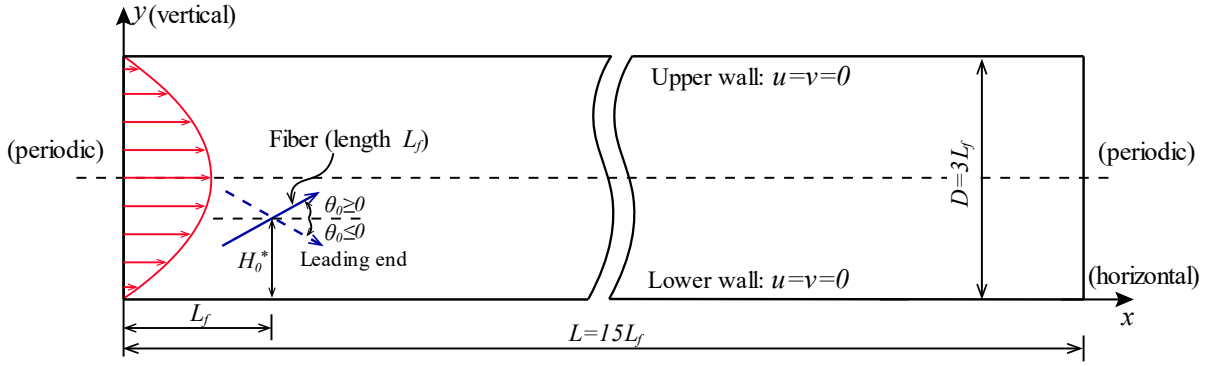

Fig.1. Schematic view of the problem and boundary conditions (the arrowhead on the fiber indicates the leading end)

The flow in our simulations is driven by a constant body force density, which is equivalent to a pressure gradient. To examine the long-term fiber dynamics the channel needs to be long enough so that the fiber can keep migrating forward. To alleviate the computational load, we assume that the conveyance system is periodic in the flow direction. That means a fiber conveyed out at the outlet will instantaneously, re-enter at the inlet. We choose a channel length of $15L_f$ so that the disturbance at the downstream will have a relatively small impact on the upstream. For the upper and lower walls, the no-slip condition is imposed. For the fiber, a free-end boundary condition is applied to both its leading and trailing ends, which reads

$$\frac{\partial^2 \boldsymbol{X}}{\partial s^2} = 0, \ \frac{\partial^3 \boldsymbol{X}}{\partial s^3} = 0 \tag{1}$$

where $\boldsymbol{X}$ is the position vector of the fiber and s its Lagrangian coordinate along the length.

The flow Reynolds number in this study is defined as

$$Re = \frac{u_m D}{\upsilon} \tag{2}$$

where u_m is the maximal velocity of the Poiseuille flow, and υ the kinematic viscosity of the fluid.

In our simulations, all quantities involved are non-dimensionalized by u_m, L_f and the density of the fluid ρ. Therefore, the non-dimensional position $\boldsymbol{X}^*$ and time t^* are

$$\boldsymbol{X}^* = \frac{\boldsymbol{X}}{L_f}, t^* = \frac{u_m t}{L_f} \tag{3}$$

For the fiber, its linear density ρ_f, stretching coefficient K_s, and bending rigidity K_b are also non-dimensionalized as follows.

$$\rho_f^* = \frac{\rho_f}{\rho L_f},\ K_s^* = \frac{K_s}{\rho {u_m}^2 L_f},\ K_b^* = \frac{K_b}{\rho {u_m}^2 {L_f}^3} \tag{4}$$

where the quantities with $*$ denote their non-dimensional counterparts.

In all the simulation cases in this paper, the chosen *Re* is 2000, indicating that the flow is laminar. The conveyance of fiber-like structures around such *Re* regime can be found in many real-life scenarios. For example, in human arteries where detached tissue debris or ruptured plaque fragments migrate in the blood stream. The fiber studied here is assumed to be light and rather compliant. Therefore, ρ_f^* and K_b^* are set as 0.6 and 3×10^{-4}, respectively in our simulations to give the fiber relatively small inertia and obvious elasticity (the dimensionless parameter that measures the relative importance of the fluid kinetic energy and fiber elasticity $\eta = \sqrt{\frac{\rho u_m^2 D^3}{2K_b}}$ is about $212 \gg 1$). The stretching coefficient is chosen as $K_s^* = 200$, a value much larger than K_b^* to enforce the inextensibility condition of fiber. Note that the fiber's dynamics may also depend on several other parameters such as ρ_f^*, K_b^* and *Re*. However, the effect of these parameters will not be covered in this paper, as we will restrict ourselves only to the initial fiber state.

3. Mathematical model and numerical implementation

3.1. Structure solver for fiber dynamics

Due to its large aspect ratio, the dynamics of fiber might be reduced to a one-dimensional description by averaging the underlying balance laws over its cross-sections. Based on the Cosserat rod theory, the governing dynamic equation for an elastic fiber is given as [37, 40]

$$\rho_f \frac{\partial^2 \boldsymbol{X}}{\partial t^2} = \frac{\partial}{\partial s}\left[T(s)\frac{\partial \boldsymbol{X}}{\partial \mathrm{s}}\right] - K_b \frac{\partial^4 \boldsymbol{X}}{\partial s^4} + \boldsymbol{F_{fluid}} + \boldsymbol{F}_c \tag{5}$$

where the first two terms of the right-hand side represent the stretching and bending forces of fiber, respectively. K_b is the bending stiffness. $\boldsymbol{F_{fluid}}$ is the hydrodynamic force exerted on the fiber, and $\boldsymbol{F}_c$ is the repulsive force due to fiber-wall collisions. The tensile force $T(s)$ reads,

$$T(s) = K_s\left(\left(\frac{\partial \boldsymbol{X}}{\partial \mathrm{s}} \cdot \frac{\partial \boldsymbol{X}}{\partial \mathrm{s}}\right)^{\frac{1}{2}} - 1\right) \tag{6}$$

where K_s is the stretching coefficient, which is given a large number in our simulation to enforce the inextensibility condition of the fiber.

The fiber is represented by a set of isometric Lagrangian point $\boldsymbol{X}(\mathrm{s}_i, \mathrm{t}), i = 0, 1, \cdots, N$, and the derivatives in the right-hand side of Eq. (1) can be discretized in space by a central finite difference (FD) formula.

$$\rho_c \frac{\partial^2 \boldsymbol{X}}{\partial t^2} = \frac{T_{i+\frac{1}{2}} \left[\frac{\partial \boldsymbol{X}}{\partial s}\right]_{i+\frac{1}{2}} - T_{i-\frac{1}{2}} \left[\frac{\partial \boldsymbol{X}}{\partial s}\right]_{i-\frac{1}{2}}}{\Delta s} - K_b \frac{\boldsymbol{X}_{i+2} - 4\boldsymbol{X}_{i+1} + 6\boldsymbol{X}_i - 4\boldsymbol{X}_{i-1} + \boldsymbol{X}_{i-2}}{\Delta s^4} + \boldsymbol{F}_{\boldsymbol{fluid}} + \boldsymbol{F}_c \tag{7}$$

where $\frac{\partial \boldsymbol{X}}{\partial s}$ is the tangent vector which is calculated at the segment center via a first-order central FD stencil.

$$\left[\frac{\partial \boldsymbol{X}}{\partial s}\right]_{i+\frac{1}{2}} = \frac{\boldsymbol{X}_{i+1} - \boldsymbol{X}_i}{\Delta s}, \text{ and } \left[\frac{\partial \boldsymbol{X}}{\partial s}\right]_{i-\frac{1}{2}} = \frac{\boldsymbol{X}_i - \boldsymbol{X}_{i-1}}{\Delta s} \tag{8}$$

with the subscript i stands the ith fiber node. Similarly, the tensile force at the segment center T is calculated by assuming the fiber a neo-Hookean material.

$$T_{i+\frac{1}{2}} = K_s \left(\left| \frac{\boldsymbol{X}_{i+1} - \boldsymbol{X}_i}{\Delta s} \right| - 1 \right), \text{ and } T_{i-\frac{1}{2}} = K_s \left(\left| \frac{\boldsymbol{X}_i - \boldsymbol{X}_{i-1}}{\Delta s} \right| - 1 \right) \tag{9}$$

The treatment of the left-hand side of Eq. (5) (the temporal discretization) requires more care, as it is closely related to the stability of the explicit structure solver whose time-marching scheme should not violate the Courant–Friedrichs–Lewy (CFL) condition. Here the third-order Runge–Kutta method is adopted to advance the position and velocity of fiber from time step n to $n + 1$.

3.2. Governing equations and Flow solver

The flow in this study is assumed to be incompressible, laminar, and Newtonian. The governing equations for the flow are given as

$$\rho \left(\frac{\partial \boldsymbol{u}}{\partial t} + \boldsymbol{u} \cdot \nabla \boldsymbol{u} \right) = -\nabla p + \mu \Delta \boldsymbol{u} + \boldsymbol{f_e} \tag{10}$$

$$\nabla \cdot \boldsymbol{u} = 0 \tag{11}$$

where $\boldsymbol{u}$ is the fluid velocity, ρ and μ are the density and dynamic viscosity of the fluid, respectively. p is the pressure and $\boldsymbol{f_e}$ is the external force from the immersed structural boundary.

In present simulations, the two-dimensional incompressible viscous flow is solved by a multi-relaxation-time lattice Boltzmann model (MRT-LBM) with a D2Q9 lattice model. The MRT-LBM has been proved to have a better stability and accuracy over the traditional lattice Bhatnagar–Gross–Krook (LBGK) or single-relaxation-time (SRT) models [41], thus is more preferable to incorporate with IBM to solve FSI problems, especially in relatively large Reynolds number (Re) flows. In the D2Q9 lattice model, the discrete velocities are,

$$\boldsymbol{e_\alpha} = \begin{cases} (0,0), & \alpha = 0 \\ c(\cos[\pi(\alpha-1)/2], \sin[\pi(\alpha-1)/2]), & \alpha = 1,2,3,4 \\ \sqrt{2}c(\cos[\pi(2\alpha-1)/4], [\pi(2\alpha-1)/4]), & \alpha = 5,6,7,8 \end{cases} \tag{12}$$

where $c = 1$ is the lattice speed and α the velocity index.

In the MRT frame, the evolution equation of the lattice Boltzmann equation is rewritten in its moment form as

$$|f(\boldsymbol{x}+\boldsymbol{e_\alpha}\Delta t, t+\Delta t)\rangle - |f(\boldsymbol{x},t)\rangle = -\mathbf{M}^{-1}\hat{\mathbf{S}}[|m(\boldsymbol{x},t)\rangle - |m^{eq}(\boldsymbol{x},t)\rangle] \tag{13}$$

where $f(\boldsymbol{x},t)$ is the velocity distribution function (VDF), representing the possibility of finding a particle in position $\boldsymbol{x}$ and time t with velocity $\boldsymbol{e_\alpha}$. The notation $|\cdot\rangle$ denotes column vector, i.e. $|f\rangle \equiv (f_0, f_1, \cdots, f_8)^T$. $|m\rangle$ is the moment column and $|m^{eq}\rangle$ its corresponding equilibrium value, and they are defined as,

$$|m\rangle = \left(\rho, e, \varepsilon, j_x, q_x, j_y, q_y, p_{xx}, p_{xy}\right)^{\mathrm{T}} \tag{14}$$

$$\begin{aligned} |m^{eq}\rangle &= \left(0,\ e^{eq}, \varepsilon^{eq}, 0, q_x^{eq}, 0, q_y^{eq}, p_{xx}^{eq}, p_{xy}^{eq}\right)^{\mathrm{T}} \\ &= \left(0, -2\rho + 3\left(j_x^2 + j_y^2\right)/\rho, \rho - 3\left(j_x^2 + j_y^2\right)/\rho, 0, -j_x, 0, -j_y, \left(j_x^2 - j_y^2\right)/\rho, j_x j_y/\rho\right)^{\mathrm{T}} \end{aligned} \tag{15}$$

where ρ is the fluid density, e the energy. j_x and j_y are the components of the moment density $\rho\boldsymbol{u}$. q_x and q_y are the energy flux components, p_{xx} and p_{xy} relate to the viscous stress tensor.

$\mathbf{M}$ is a 9×9 transformation matrix which defines the mapping between f and m, i.e., $|m\rangle = \mathbf{M}|f\rangle$, $\hat{\mathbf{S}}$ is the non-negative 9×9 diagonal collision matrix, which is defined as following in the D2Q9 velocity model.

$$\hat{\mathbf{S}} \equiv diag\{s0, s1, s2, s3, s4, s5, s6, s7, s8\} \tag{16}$$

where $s0 = s3 = s5 = 0, s1 = 1.64, s2 = 1.54, s4 = s6 = 1.9$, and $s7 = s8 = 1/(3\nu/\Delta t + 0.5)$. Here ν is the kinematic viscosity of the fluid, which is decided by the Re.

In the current MRT frame, the effect of external force $\boldsymbol{f_e}(\boldsymbol{x},t)$ on the fluid is included through two steps. Firstly, add one-half of $\boldsymbol{f_e}(\boldsymbol{x},t)\Delta t$ to the moment flux j_x and j_y before the collision, then add another half after the collision.

3.3. Fluid-structure interaction

The interaction between the fiber and the flow is solved by the immersed boundary method (IBM). In the last several decades, the IBM has been successfully combined with the LBM and evolved into various variants [42]. Here, we adopt a version proposed by Niu et al. [43], which is straightforward to implement and powerful in handling both rigid and elastic immersed boundaries. In this version, the hydrodynamic force is evaluated by the momentum exchange scheme on the VDF $f_\alpha(\boldsymbol{X},t)$ at the boundary. As the Lagrangian grid points may not coincident with the Eulerian grid points, the VDF at the boundary points needs to be interpolated [30].

$$f_\alpha(\boldsymbol{X},t) = \sum_{\boldsymbol{x}} f_\alpha(\boldsymbol{x},t)\sigma_h(\boldsymbol{x}-\boldsymbol{X})\,h^2 \tag{17}$$

where $\sum_x$ denotes the summations over all Eulerian grid points, and h is the Eulerian grid spacing. $\sigma_h(\cdot)$ is the smoothed Dirac delta function which takes the following form in our simulations.

$$\sigma_h(\boldsymbol{x}-\boldsymbol{X}) = \frac{1}{h^2}\emptyset\left(\frac{x-X}{h}\right)\emptyset\left(\frac{y-Y}{h}\right) \tag{18}$$

with the four-point $\emptyset(r)$ being

$$\emptyset(r) = \begin{cases} \left(3-2|r|+\sqrt{1+4|r|-4r^2}\right)/8, & |r| \le 1 \\ \left(5-2|r|-\sqrt{-7+12|r|-4r^2}\right)/8, & 1 \le |r| \le 2 \\ 0, & |r| \ge 2 \end{cases} \tag{19}$$

Based on the interpolated $f_\alpha(\boldsymbol{X},t)$ at the boundary, a new set of VDF is obtained by applying the bounce-back rule, i.e.,

$$f_{-\alpha}(\boldsymbol{X},t+\Delta t) = f_\alpha(\boldsymbol{X},t) - 2\omega_\alpha\rho\frac{\boldsymbol{e}_\alpha\boldsymbol{U}(\boldsymbol{X},t)}{c_s^2} \tag{20}$$

where $-\alpha$ denotes the opposite direction of α. $\boldsymbol{U}(\boldsymbol{X},t)$ is the boundary velocity, $c_s = \sqrt{3}c/3$ the speed of sound in LBM, and ω_α is the weighting coefficient given as: $\omega_0 = 4/9$, $\omega_{1,2,3,4} = 1/9$ and $\omega_{5,6,7,8} = 1/36$.

The hydrodynamic force exerted on the boundary points can be computed via momentum exchange scheme,

$$\boldsymbol{F_{fluid}}(\boldsymbol{X},t) = -\sum_\alpha \boldsymbol{e}_\alpha\,[\,f_\alpha(\boldsymbol{X},t+\Delta t) - f_{-\alpha}(\boldsymbol{X},t)] \tag{21}$$

and its reaction force $-\boldsymbol{F_{fluid}}(\boldsymbol{X},t)$ further be distributed to the background fluid,

$$\boldsymbol{f_e}(\boldsymbol{x},t) = -\sum_{\boldsymbol{X}} \boldsymbol{F_{fluid}}(\boldsymbol{X},t)\sigma_h(\boldsymbol{x}-\boldsymbol{X})\Delta s \tag{22}$$

where Δs is the Lagrangian grid spacing and $\sum_{\boldsymbol{X}}$ denotes the summations over all the Lagrangian grid points.

3.4. Fiber-wall collisions

To prevent a fiber from penetrating the sidewalls during the simulation, the effect of fiber-wall collision must be included. In this study, this collision is solved by introducing a short-range repulsive force which is a result of fluid lubrication when two immersed objects are in close proximity. In IBM, this repulsive force can be calculated conveniently using the smooth Dirac delta function [28].

$$\boldsymbol{F}_c(\boldsymbol{X},t) = \int_0^L \sigma_h(\boldsymbol{X}-\boldsymbol{X}')\frac{\boldsymbol{X}-\boldsymbol{X}'}{|\boldsymbol{X}-\boldsymbol{X}'|}ds' \tag{23}$$

where $\boldsymbol{X}$ is the position of the fiber node where the repulsive force is acting, and $\boldsymbol{X}'$ is the position vectors of the corresponding fiber or wall nodes that are at close range to $\boldsymbol{X}$.

4. Numerical validations

The validity of our coupled fluid-structure interaction (FSI) solver was validated against three benchmark problems. First, the structure solver was validated by simulating the swinging motion of a flexible rope pendulum under gravity. Then the boundary force evaluation scheme was verified by simulating the flow over a stationary circular cylinder. The third validation case simulated the flapping motion of a filament in a uniform flow to verify the effectiveness of our algorithm in solving FSI problem. Apart from that, grid and time-step independence studies were carried out to make sure that the solution is independent of the grid resolution and time step adopted.

4.1. A flexible rope pendulum swings under gravity

The schematic diagram is shown in Fig. 2a. A flexible pendulum is pivoted and initially hanging sideways (initial angle $= \theta$) from the vertical direction where gravity $\mathbf{g}$ applies. Both the length L and linear density ρ_f of the pendulum are set to unit, and the value of gravity $|\mathbf{g}|$ is chosen as 10. The dynamics of the pendulum is governed by Equation (5) with the hydrodynamic and repulsive forces being replaced by a gravity, and the equation is solved by our structure solver with a typical result demonstrated in Fig. 2b, where the swinging motion shows asymmetrical features due to the flexibility of the pendulum. When θ is very small, the analytical solution for the tip displacement of the swinging pendulum can be derived using a perturbation method [28], which yields (a hinged and a free-end boundary condition are considered)

$$x(s,t) = \sum_{i=1}^{\infty} \frac{4\theta L}{z_i^2} \frac{J_2(z_i)}{J_1^2(z_i)} J_0\left(z_i \sqrt{\frac{L-s}{L}}\right) \cos\left(\frac{z_i}{2}\sqrt{\frac{|\mathbf{g}|}{L}}\right) \tag{24}$$

where J_0, J_1 and J_2 are the Bessel function of the first kind of order zero, one and two, respectively. z_i is the *i-th* positive root of $J_0(z)$.

For a totally flexible pendulum ($K_b = 0$) with a small initial angle ($\theta = 0.01$), the comparison of the simulated and analytically calculated tip x-displacement at successive time is shown in Fig. 2c, which shows a good agreement between our numerical and analytical results.

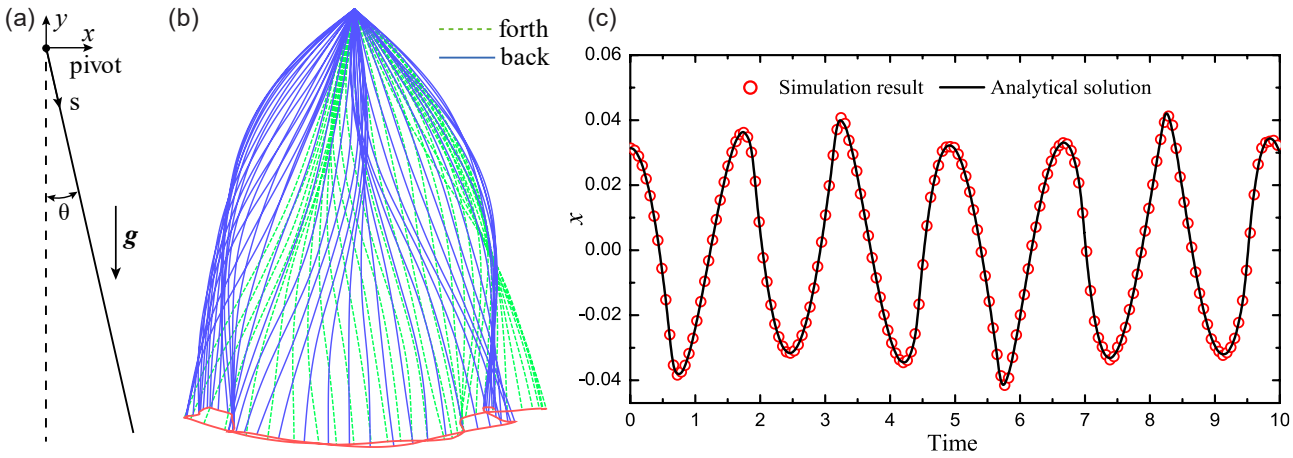

Fig. 2. The schematic diagram of the swinging pendulum problem (a) simulated superposition of the pendulum in one cycle ($K_b = 1 \times 10^{-3}, \theta = 0.15\pi$) (b) comparison of the tip x-displacement between numerical and analytical solutions ($K_b = 0, \theta = 0.01$) (c)

4.2. Flow over a circular cylinder

A stationary cylinder with a diameter of D_c is placed in the central line of a $40D_c \times 40D_c$ domain, and the downstream in $24D_c$ long. The surface of the cylinder is represented by 120 uniformly distributed Lagrangian points while D_c covers 30 Eulerian grids. The far-field boundary condition is imposed at the boundaries of the domain. The flow at four Reynolds numbers $Re = 20, 40, 100$ and 200, is simulated using our current FSI solver. The Re here is defined as

$$Re = \frac{u_\infty D_c}{\upsilon} \tag{25}$$

where u_∞ is the velocity of the incoming flow stream, and υ the kinematic viscosity of the flow. The average drag coefficients C_d, lift coefficients C_l and Strouhal number St are calculated for comparison with the literature data, and they are defined as

$$C_d = \frac{F_d}{0.5\rho u_\infty^2 D_c}, \text{and } C_l = \frac{F_l}{0.5\rho u_\infty^2 D_c} \tag{26}$$

$$St = \frac{f D_c}{u_\infty} \tag{27}$$

where F_d and F_l are the drag force and lift force the fluid exerted on the cylinder, respectively, and f is the vortex shedding frequency which is evaluated using fast Fourier transform (FFT).

Comparisons of C_d, C_l and St with those in the literature are shown in Table 1, where a favorable agreement is obtained.

Table 1. Comparison of C_d, C_l and St with those from the literature

References	C_d				C_l/St	
	$Re = 20$	$Re = 40$	$Re = 100$	$Re = 200$	$Re = 100$	$Re = 200$
Tian et al. [29]	2.16	1.62	1.43	1.44	−/0.166	−/0.198
Xu et al. [44]	2.23	1.66	1.42	1.42	±0.34/0.171	±0.66/0.202
Russell et al. [45]	2.22	1.63	1.43	1.45	±0.339/0.175	±0.75/0.202
Yuan et al. [30]	2.069	1.559	1.397	1.397	±0.338/0.160	±0.672/0.190
Present study	2.160	1.620	1.444	1.440	±0.348/0.160	±0.701/0.193

4.3. Flapping filament in a uniform flow

We further validated the effectiveness of our FSI algorithm by simulating a well-studied flapping-filament problem. The filament is placed in a uniform flow of $10L \times 8L$ with its upstream end tethered at ($3L$, $4L$). The bending rigidity of the filament is chosen as $K_b^* = 1 \times 10^{-3}$ and the *Re* is 165. The mass ratio of the filament is varied to examine its possible dynamics pattern. Previously studies have demonstrated that there is a critical mass ratio, below which the filament eventually rests in straight state aligning with the flow [27, 30, 37, 46]. Our simulated results are shown in Fig.3, which predicts a critical mass ratio between 0.12-0.16. This is in good agreement with the theoretic work of Connell & Yue [37], where the predicted critical mass ratio was around 0.14 at $K_b^* = 1 \times 10^{-3}$, and *Re*=165. The comparison between our results and that of Yuan et al. [30] is shown in Table 2, where a reasonable agreement is obtained.

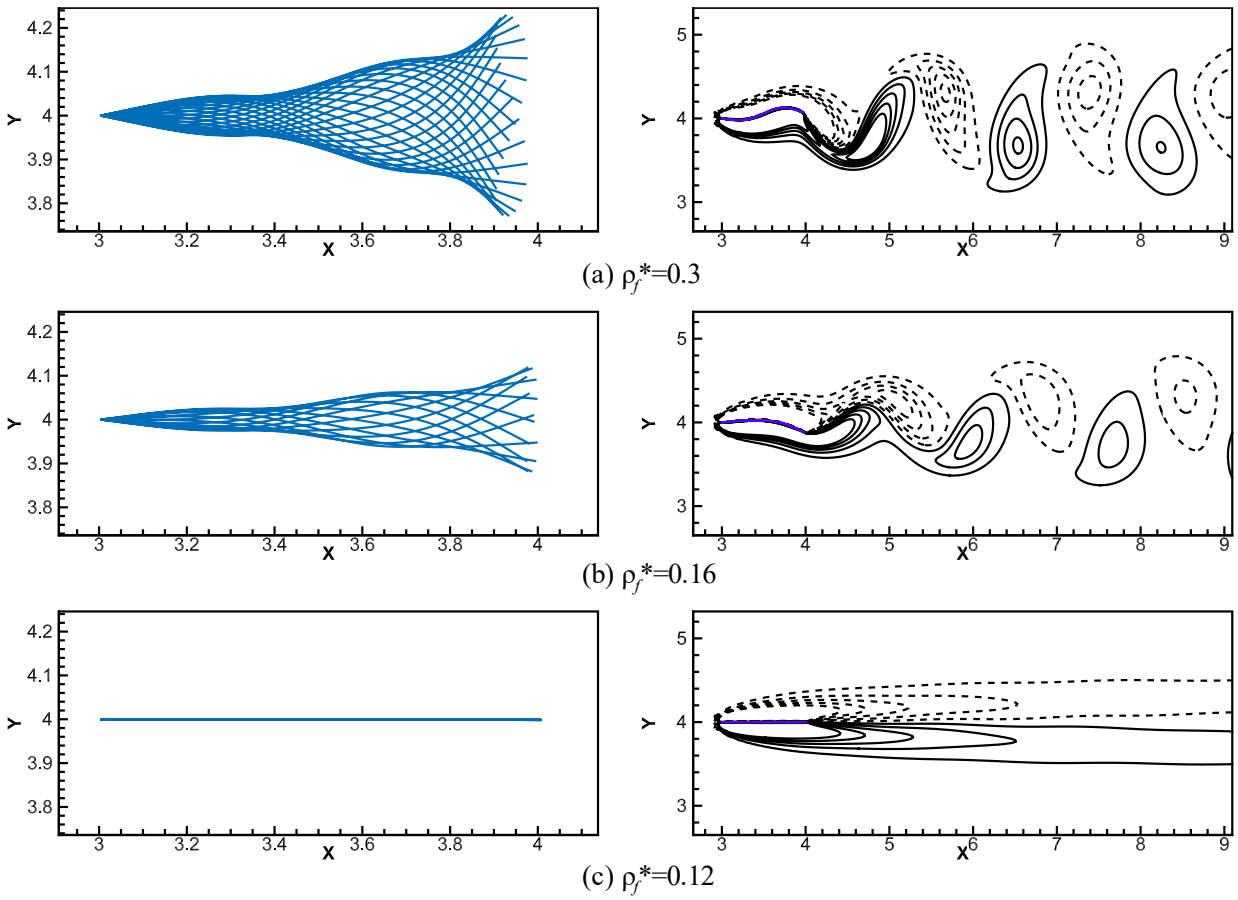

Fig. 3 Simulated superposition of the filament (left) and vorticity contour at t^*=130 (right) at various ρ_f^*

Table 2. The flapping amplitude, C_d and St at Re=165, $K_b^* = 1 \times 10^{-3}$, and $\rho_s^* = 0.3$

Sources	Amplitude	C_d	St
Yuan et al. [30]	0.43	0.425	0.489
Present	0.447	0.452	0.465

4.4. Grid and time-step independence study

We performed the grid and time-step independence study by simulating the conveyance of a single fiber in a short channel ($L = 5L_f$) at various grid sizes and time steps. The fiber is initially placed at $H_0^* = 0.5, \theta_0 = 90^\circ$. The flow Re is 2000 and the Lagrangian grid spacing Δs is set equal to the Eulerian grid spacing Δx. Starting from the coarsest grid, the grid size is refined by a factor of 1.5 in each simulation case that follows. The dimensionless conveyance time T^* it takes to deliver the vertically placed fiber to the channel outlet and the conveyance speed U^* (u-veolicty of fiber's middle point) at that moment are tabulated and made comparison

among different grid levels, as shown in Table. 3. It can be seen that this quantity is convergent as the grid gets refined, and in the cases when $\Delta x^* \geq 1/100$, a very small difference (less than 0.2%) in both T^* and U^* can be observed. Therefore, in our fiber conveyance simulations, a grid size of $\Delta x^* = 1/100$, and time step of $\Delta t^* = 1 \times 10^{-3}$ are chosen to save computational cost.

Table 3. Comparison of the conveyance time T^* and conveyance speed U^* at the outlet among different grid spacing and time steps

Grid spacing Δx^*	Time step Δt^*	Conveyance time T^*	Conveyance speed U^* at channel outlet
$1/66$	1×10^{-3}	11.444	0.8852
$1/100$	1×10^{-3}	11.448	0.8857
$1/150$	1×10^{-3}	11.448	0.8858
$1/100$	5×10^{-4}	11.461	0.8867

5. Results and Discussion

5.1. Fiber initially aligned with the flow direction released at various vertical positions H_0^*

We first consider the conveyance of a single fiber that initially aligned with the flow direction (i.e. horizontally placed, $\theta_0 = 0^\circ$). To investigate the effect of released positions on fiber dynamics, the initial vertical position H_0^* is set as 0.1, 0.2, 0.3, 0.4 and 0.5, respectively. In our study, the fiber's vertical position and conveyance (U-velocity component) speed are evaluated at its middle point. To describe fiber's deformation, a bending factor γ is defined, which is the ratio of fiber's end-to-end distance to its undeformed length L_f ($\gamma \leq 1$, and $\gamma = 1$ indicates that the fiber is totally straight).

The evolution of the fiber's configuration at the initial stage is shown in Fig. 4, where $Y^*=y/L_f$ is the dimensionalized y-coordinate. It can be seen that among all the five cases, only the fiber that placed at the centerline of the channel (i.e. $H_0^* = 0.5$) manages to travel forward along a horizontal path without getting deformed or reoriented. For all the other four cases (i.e. $H_0^* \neq 0.5$), the paths deviate from the horizontal and deformation and reorientation of the fiber are observable in the upstream. Furthermore, when $H_0^* \neq 0.5$, the fiber is observed to first move towards the near sidewall (sideway drift), which later induces fiber-wall collisions. When the fiber is placed at the channel centerline, the top-bottom symmetry of the system is well

maintained, and no vertical hydrodynamic load will be exerted on the fiber. Placing the fiber elsewhere will break this symmetry and leads to instability of the system. More specifically, it will gradually generate vertical hydrodynamic load at the fiber. This load, as shown in Fig. 5, is time-varying and not uniformly distributed. It will bend the fiber at the trailing section and cause a sideway drift motion. A similar sideway drift motion was also observed in Zhu [33], where the inhomogeneous properties of the filament and external disturbances work as sources for the instability. In Fig. 4, we can also see that after the fiber-wall collisions, there are two typical ways for the fiber to leave the wall. In the first way, the fiber's trailing end will be lifted first, which then causes the fiber to tumble forward and the fiber is observed to leave the wall very quickly. In the second way, the fiber is less deformed, and its trailing end keeps contacting with the wall. In this case, the fiber leaves the wall slowly with an inclined configuration. Fig. 6 shows the streamlines at several selected timesteps for various H_0^*. In the case of $H_0^* = 0.1$ and 0.2, vortexes are generated when a fiber-wall collision occurs. Compared with that in the initial stage, the streamline in the far downstream appears to be less affected by the fiber indicating that the fiber has a low flow resistance when it gets fully settled in the flow field. The streamlines are also found to penetrate the fiber as we represent the fiber with only one layer of grid in our simulations (i.e., the fiber has a thickness of one grid spacing).

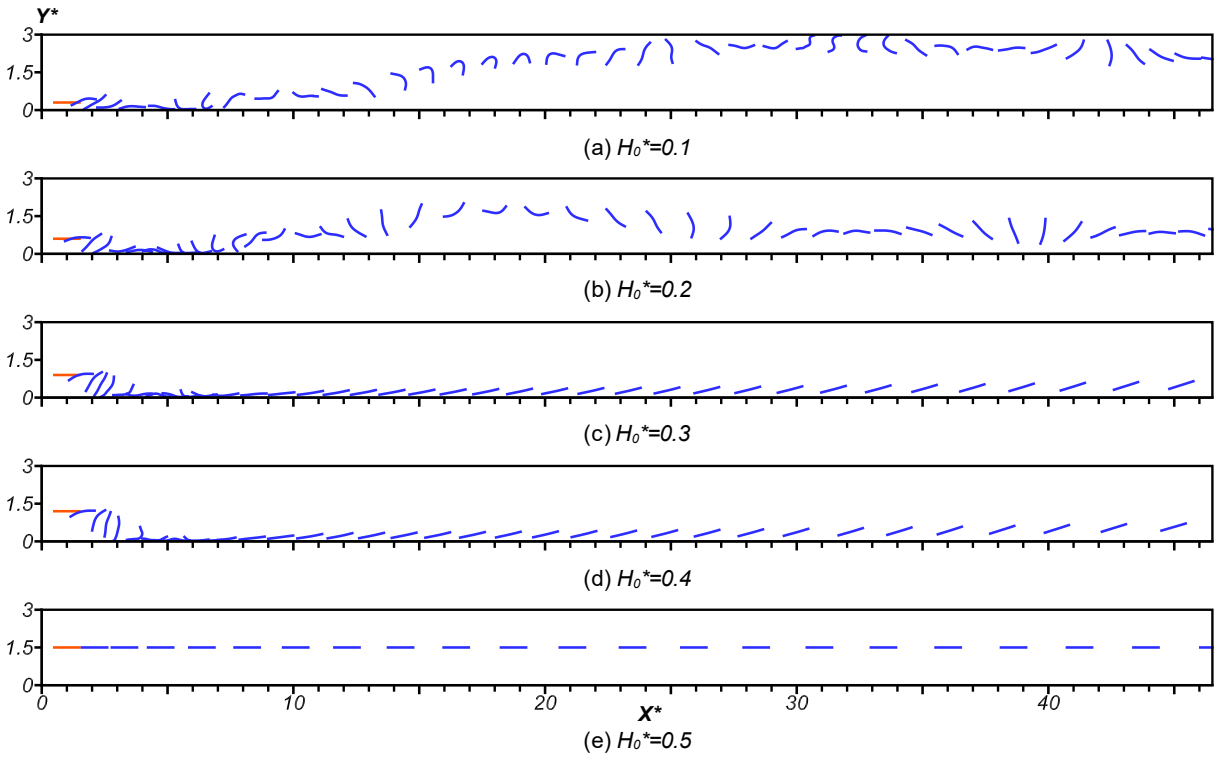

Fig. 4. Evolution of the fiber's configurations at the initial stage for various H_0^*

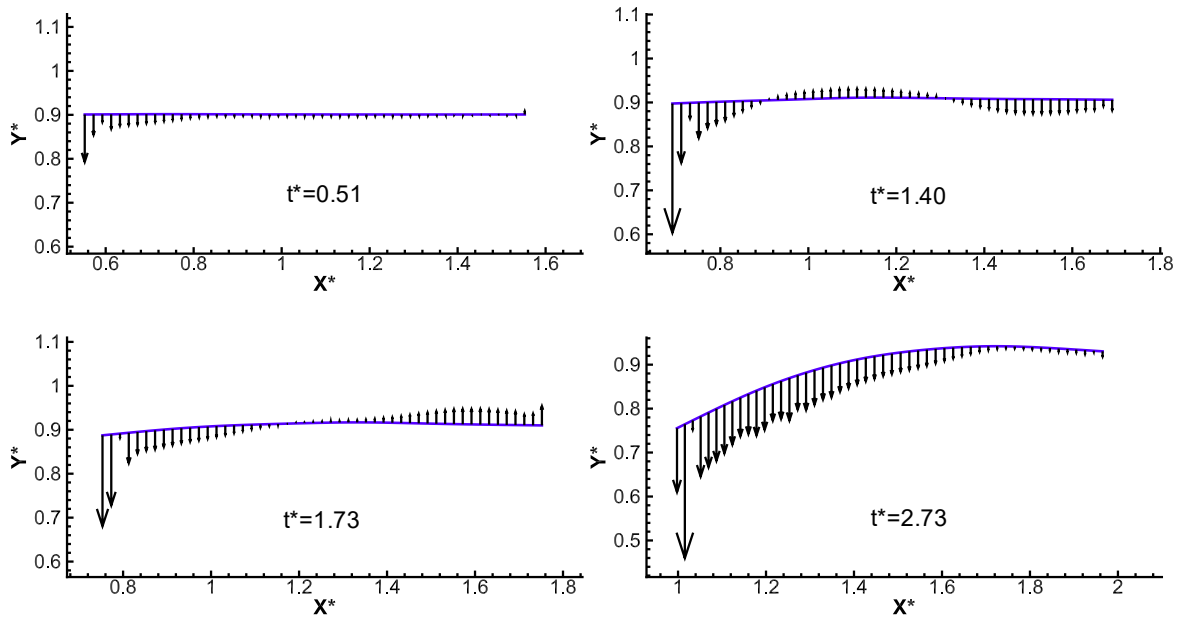

Fig. 5. The distribution of the vertical component of the hydrodynamics load for $H_0^* = 0.3$ at different moments

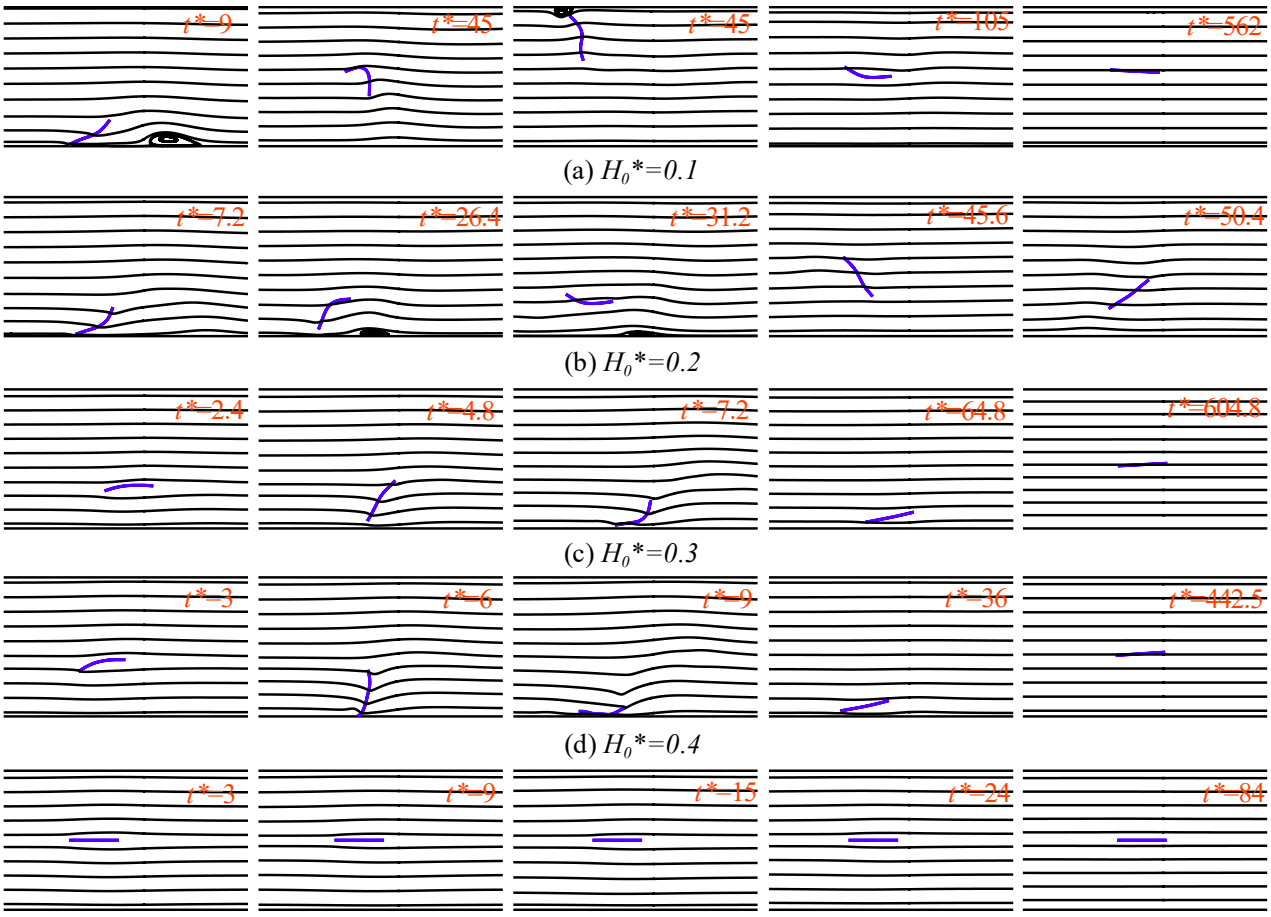

Fig. 6. The streamlines at several selected timesteps for various H_0^* (streamlines plotted based on the absolute flow velocity)

The time evolutions of the end-to-end orientation and bending factor for various H_0^* are shown in Fig. 7. In the cases of $H_0^* = 0.1, 0.3, 0.4$ and 0.5, though fluctuations may arise in the upstream, the fibers' orientations eventually stabilize at values that very close to zero, meaning that the fibers eventually nearly align with the flow and translate forward. For these cases, the fibers also tend to be straight in the far downstream, as their bending factor approach unity as shown in Fig. 7b. The fibers in these cases attain their equilibrium states in the downstream, and their equilibrium configurations are shown in Fig. 8a. In contrast, no equilibrium state is observable for the fiber initially placed at $H_0^* = 0.2$. Instead, it is found to do a tumbling motion, which becomes periodic in the downstream (this can be observed from the flips shown in Fig. 7a, when a flip takes place, the end-to-end orientation becomes discontinuous). A typical tumbling motion is presented in Fig. 8b. During the tumbling process, the fiber is also observed to buckle into a shallow arc thereby undergoes a springy deformation [8]. The tumbling of fiber in a Poiseuille flow has also been reported in [47, 48]. In the cases that

the fiber initially aligned with the flow, the tumbling motion may be triggered by a severe fiber-wall collision which brings the fiber a large rotational kinetic energy (a small rotational kinetic energy may eventually be damped out by the flow and the fiber will translate forward as in the case of H_0^*=0.1, where the fiber tumbles only for a short period at the beginning). The tumbling motion is maintained in the downstream by the rotational component of the local shear rate, as shown in Fig. 9a. The streamlines based on the absolute and relative velocity field are given in Fig. 9a and b, respectively. In the translation cases, when the fiber eventually gets stable, the presence of fiber seems to have a negligible effect on the flow field (see Fig. 10).

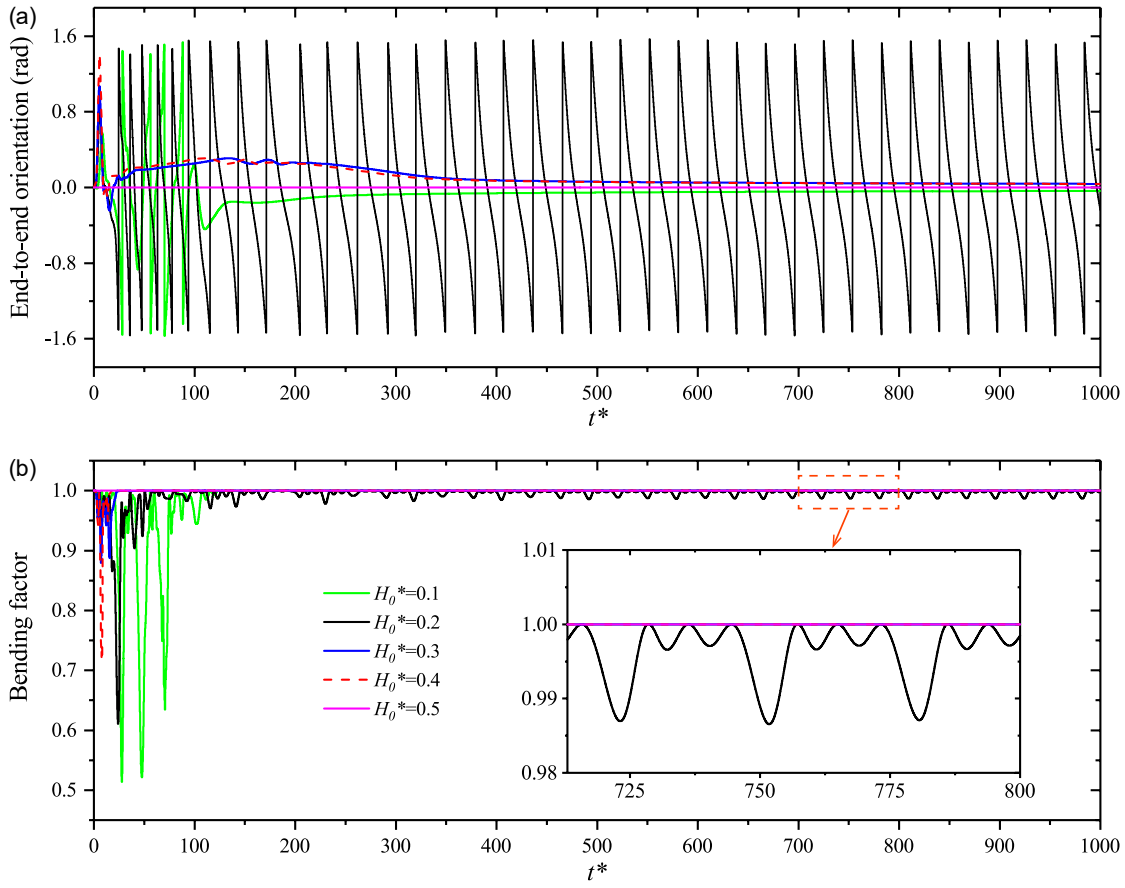

Fig. 7. The time evolutions of the end-to-end orientation (a) and bending factor (b) for various H_0^*

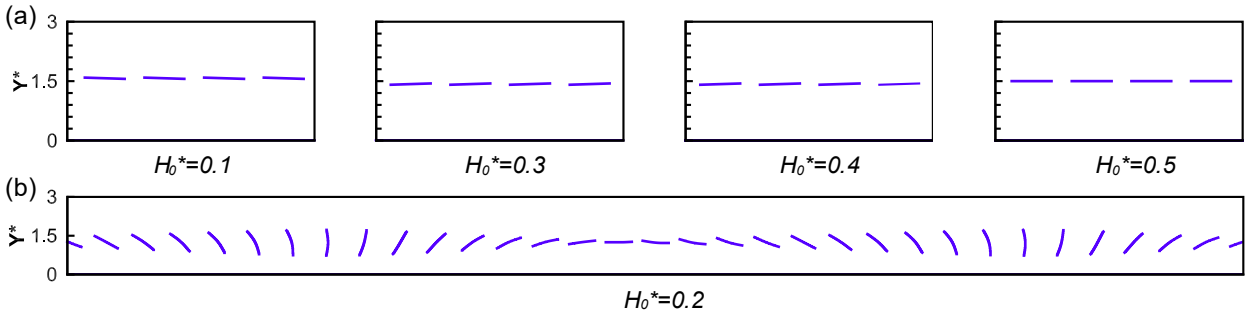

Fig. 8. The equilibrium states observed at the far downstream for fiber placed at various H_0^* (a) a typical tumbling motion for fiber placed at $H_0^* = 0.2$ (b)

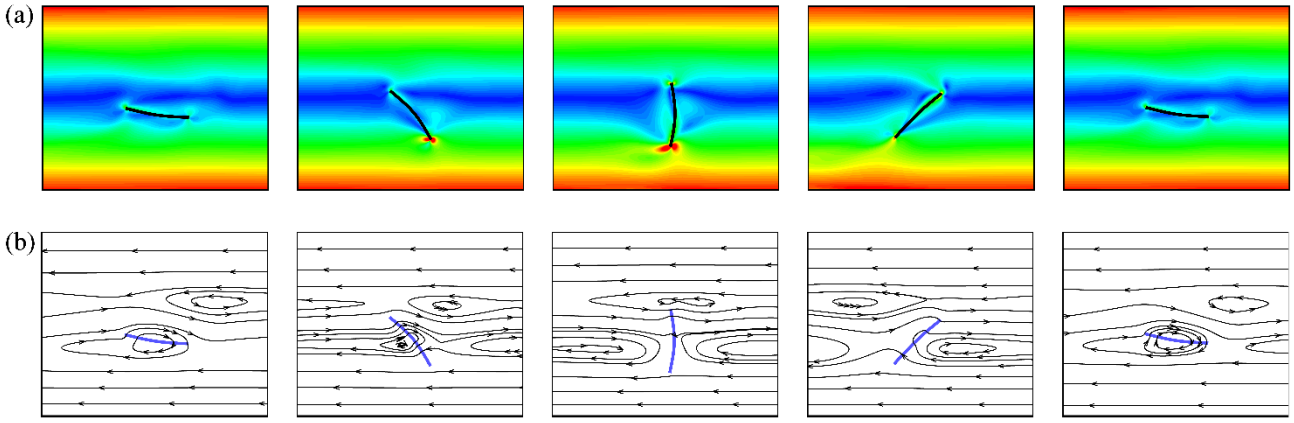

Fig. 9. Snapshots of the shear rate contour in a tumbling cycle (b) the corresponding streamlines based on the relative velocity between the flow and the fiber

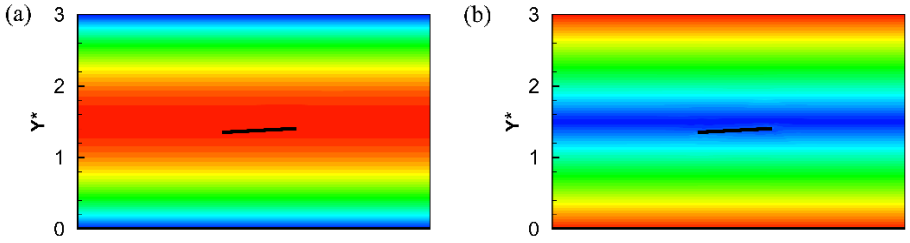

Fig. 10. The dimensionless u-velocity (a) and shear rate (b) contours in the far downstream for $H_0^* = 0.3$

The time evolutions of the fiber's vertical position for various H_0^* are shown in Fig. 11a. Interestingly, though some fibers drift to the near-wall region in the upstream, there is a trend for them to migrate laterally to the channel central region in the downstream. This phenomenon has also been observed by Słowicka et al. [48], where the effect of several parameters on this phenomenon was investigated in their study. We also notice that when the lateral migration has been completed, the fiber will eventually remain at a vertical position

slightly away from the centerline of the channel. This is consistent with the low-Reynolds-number results of Farutin et al. [47], where the authors predicted accumulation positions more or less away from the centerline. Moreover, for a fiber not placed at the centerline, we observe an off-centerline distance around 0.07 at the downstream for the fiber that translate forward, while a much larger distance of 0.26 is found for the tumbling case. The time evolution of the conveyance speed is shown in Fig. 11b, where large fluctuations in the conveyance speed are observable for cases with $H_0^* \neq 0.5$. These fluctuations typically occur at the upstream and are likely caused by the sideway drift motion and fiber-wall collisions. After a rapid acceleration process, all the fibers reach their terminal conveyance speeds and preserve those speeds in the rest journey. In the translation cases, the fibers' terminal conveyance speeds are very close to the maximal velocity of the Poiseuille flow u_m, while in the tumbling case, the conveyance speed keeps fluctuating in the downstream, and is 5% lower compared to that in the translation cases. This is because a tumbling fiber tends to settle at a position further away from the centerline (i.e. it has a larger off-centerline distance), where the local flow velocity is lower. The eventual conveyance speeds, off-centerline distances, and tumbling cycles for various H_0^* are summarized in Table 4.

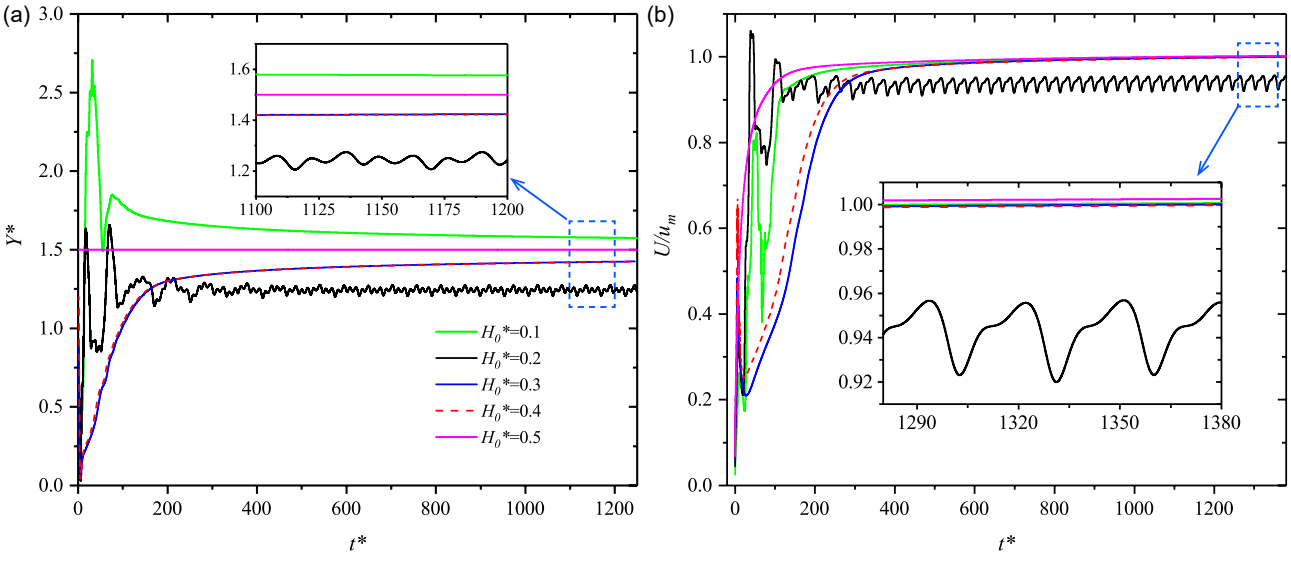

Fig. 11. The time evolutions of the vertical position (a) and conveyance speed (b) of the fiber for various H_0^*

Table 4. The eventual conveyance speeds, off-centerline distances, and tumbling cycles for various H_0^*

H_0^*	Long-term dynamics pattern	Eventual conveyance speed U/u_{max}	Eventual distance to the centerline	Tumbling cycle T^* at far downstream

0.1	Translation	1.00	0.072	/
0.2	Tumbling	0.95	0.256	28.76
0.3	Translation	1.00	0.075	/
0.4	Translation	1.00	0.075	/
0.5	Translation	1.00	0	/

5.2. Fiber released at vertical position $H_0^* = 0.5$ with various initial orientations θ_0

In this section, the fiber we simulated is no longer horizontally placed but is tilted at $H_0^* = 0.5$. Due to the symmetry of the problem, the initial orientation θ_0 is chosen as 15°, 30°, 45°, 60°, 75°, and 90°, respectively. All the other parameters remain the same as in Section 5.1.

The evolutions of the fiber's configuration in the upstream are presented in Fig. 12. We can see, the fiber drift to the sideway in all the cases except $\theta_0 = 90°$ due to the non-zero y-component of the pressure drag. The sideway drift motion further causes fiber-wall collisions and fiber slip motion in the case $\theta_0 = 60°$. The slip motion significantly reduces fiber conveyance speed but helps to straighten the fiber. Fig. 13 shows the streamlines at several selected timesteps for various θ_0, and Fig. 14 plots the time evolutions of the fiber's end-to-end orientation for different θ_0. The fibers with initial orientations $\theta_0 = 60°$, 75°, and 90° are found to translate forward with a nearly zero orientation in the downstream. In the case that the fiber is vertically placed (i.e. $\theta_0 = 90°$), it is found that the fiber remains its vertical orientation for a period of time in the upstream, during which, the fiber is slightly buckled, and the symmetry of the system is maintained (see Fig. 12f). However, when t^* is around 200, instability is triggered. The system is found to gradually lose its symmetry, and the fiber's orientation starts to vary (see this process in Fig. 15). This is different from the symmetry case we studied in Section 5.1 (i.e. the case when the fiber is initially horizontally placed at the channel centerline), where the system remains stable and symmetric throughout the conveyance. This suggests that this nonlinear system may be easier to lose stability when a fiber is vertically placed in a symmetric system. A symmetric system with a horizontally placed fiber, however, may be more stable and can withstand disturbances at higher levels. For the cases $\theta_0 = 15°$, 30°, and 45°, the fibers are observed to do periodic tumbling motions in the downstream (see Fig. 14b). Interestingly, the tumbling cycles T^* we observed are nearly identical (around 29) for all the θ_0 and H_0^* considered in this study, indicating that they may not affected by the initial orientation or vertical position of the fiber, but are likely controlled by some other parameters.

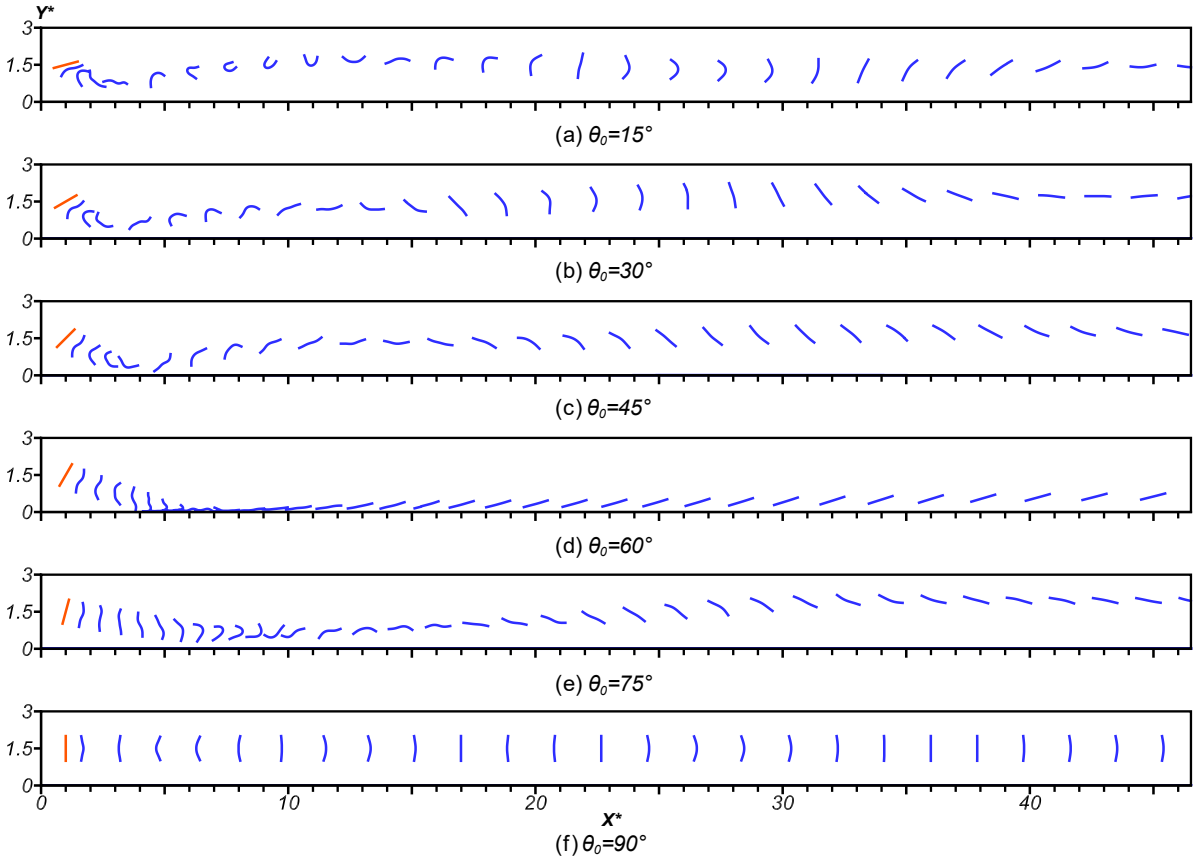

Fig. 12. Evolutions of the fiber's configurations at the initial stage for various θ_0

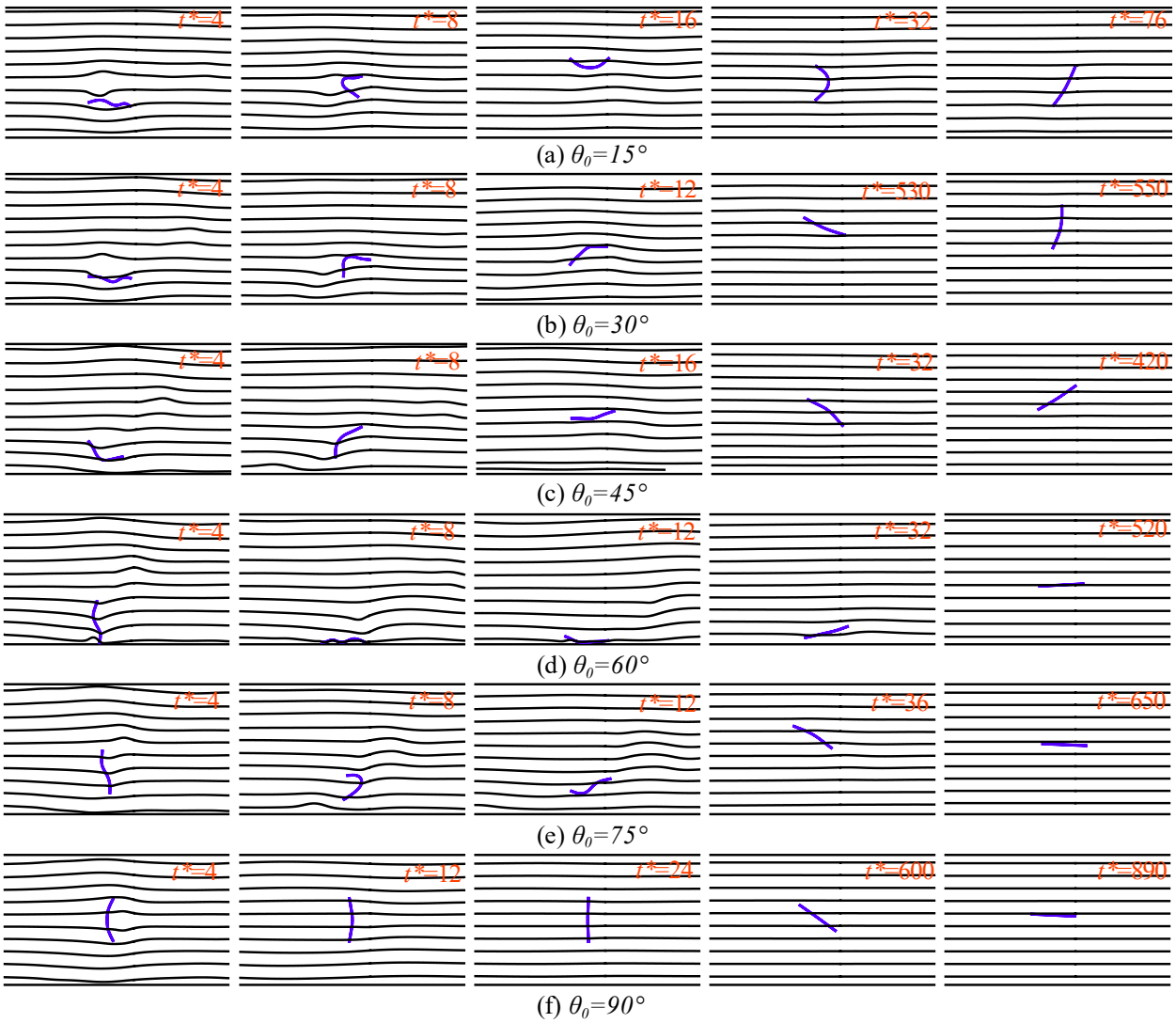

Fig. 13. The streamlines at several selected timesteps for various θ_0 (streamlines plotted based on the absolute flow velocity)

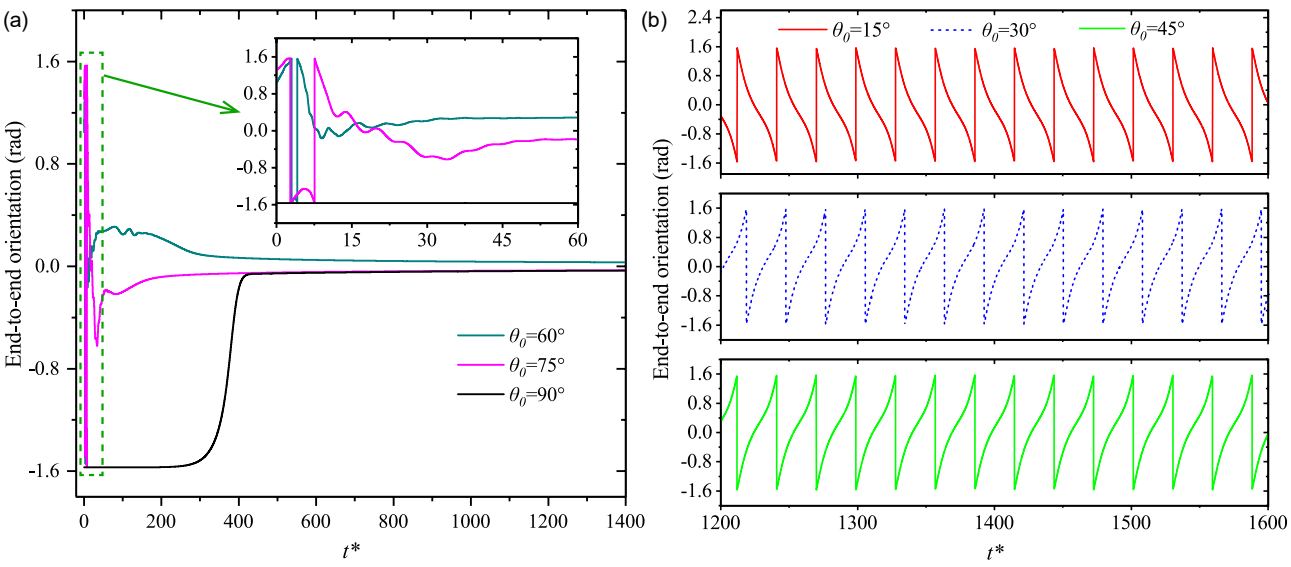

Fig. 14. The time evolutions of fiber's end-to-end orientation for various θ_0

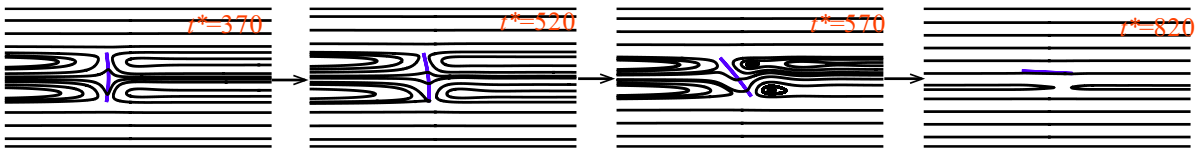

Fig. 15. Loss of the system stability and symmetry during the conveyance in the case of $\theta_0 = 90°$ (streamlines plotted based on the relative velocity between the flow and the fiber)

The time evolutions of the vertical position and conveyance speed for various θ_0 are given in Fig. 16. All the fibers are observed to deviate from the horizontal path in the upstream. However, the deviations are found to be corrected in the downstream as the fibers migrate towards the central region. In the translation cases, the fibers eventually reach to their equilibrium vertical positions, while in the tumbling cases, the fibers would fluctuate slightly around some mean values. The off-centerline distances are calculated and tabulated in Table 5. For all the tumbling cases, the distances are around 0.26, a value much larger than that in the translation cases. As no apparent difference appears in the off-centerline distance for the fibers with same dynamics pattern (translation or tumbling), we can say the eventual vertical position is dynamic-pattern dependent for a chosen conveyance system, rather than directly correlates with the specific orientation angle or vertical position. For the conveyance speed, similar result is found as in the vertical position cases studied in Section 5.1. The fiber's eventual conveyance speed depends on its vertical position and corresponds well with the local flow velocity. In the translation cases, the fibers are eventually close to centerline, therefore their terminal conveyance speeds are close to the maximal flow velocity. In the tumbling cases, the fibers have larger off-centerline distances,

thus they have lower conveyance speeds.

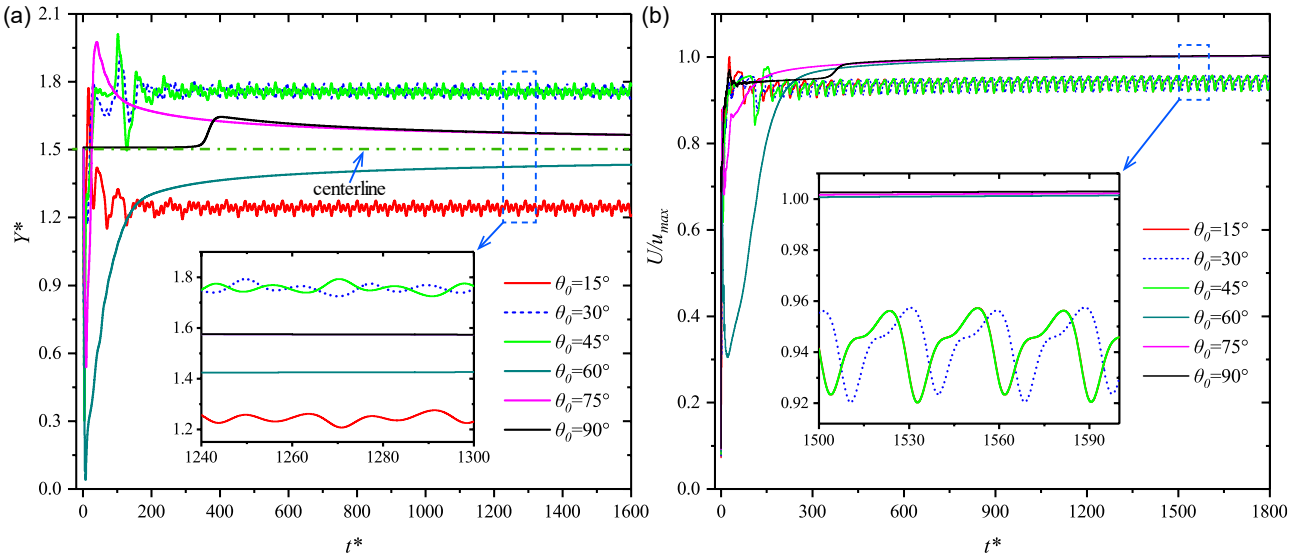

Fig. 16. The time evolutions of the vertical position (a) and conveyance speed (b) for various θ_0

Table 5. The eventual conveyance speeds, off-centerline distances, and tumbling cycles for various θ_0

θ_0	Long-term dynamics pattern	Eventual conveyance speed U/u_{max}	Eventual distance to the centerline	Tumbling cycle T^* at the downstream
15°	Tumbling	0.94	0.255	28.91
30°	Tumbling	0.94	0.257	28.96
45°	Tumbling	0.94	0.257	28.97
60°	Translation	1.00	0.065	/
75°	Translation	1.00	0.062	/
90°	Translation	1.00	0.062	/

6. Conclusions

In this study, numerical simulations are performed to investigate the effect of fiber's initial vertical position and orientation on its dynamics in a channel flow at Re=2000. The immersed boundary-lattice Boltzmann method is adopted to solve the fluid-fiber interaction, and a short-range repulsive force is introduced to model fiber-wall collisions. For the conveyance system we considered, the following conclusions can be drawn based on our simulation results:

1. The initial vertical position and orientation both could impact the fiber's dynamic pattern and equilibrium state. The fiber is found to go straight forward along a horizontal path when it is aligned with the flow and symmetrically placed at the channel centerline. Breaking this symmetry by slightly offsetting the fiber's initial vertical position from the channel centerline or tilting the fiber will induce the instability of the system, which then leads to deviations and fluctuations in fiber's conveyance path. Interestingly, despite this deviation, the fiber is observed to gradually migrate towards the channel central region in the downstream. The vertical position that a fiber eventually settles may be slightly away from the channel centerline and the off-centerline distance is dynamic-pattern dependent. Typically, we find an off-centerline distance around 0.25 for tumbling cases, and around 0.07 for translation cases (not include the symmetry case with $H_0^* = 0.5$ and $\theta_0 = 0$).
2. By varying the initial fiber states, we observed two kinds of dynamic patterns in the downstream channel. In the first pattern, the fiber eventually reaches its equilibrium state and is observed to translate forward. In the second pattern, no equilibrium state can be observed, and the fiber is found to do a tumbling motion with a constant period. The tumbling cycle is found to be independent of the initial fiber state and is about 29 for the considered system. Generally, when a fiber reaches its equilibrium state, it will have a straight configuration and a zero (or almost zero) orientation.
3. The fiber's eventual conveyance speed depends on the vertical position it eventually settles and can be roughly approximated by the local flow velocity. Therefore, fibers in translation cases can eventually obtain a larger conveyance speed due to its smaller off-centerline distance.

Acknowledgements

This work was supported by National Natural Science Foundation of China [Grant No. 51976200]; and the Hong Kong Polytechnic University [PolyU UAHL and RKC1].

References

[1] Kong, LX, Platfoot, RA. Fibre transportation in confined channel with recirculations, Comput Struct. 78 (2000) 237-45.

[2] Lawrence, CA, Chen, KZ. A study of the fiber-transfer-channel design in rotor-spinning .1. The fiber trajectory, J Text Inst. 79 (1988) 367-92.

[3] Lawrence, CA, Chen, KZ. A study of the fiber-transfer-channel design in rotor-spinning .2. Optimization of the transfer-channel design, J Text Inst. 79 (1988) 393-408.

[4] Anczurowski, E, Mason, SG. Particle Motions in Sheared Suspensions. XXIV. Rotation of Rigid Spheroids and Cylinders. 12 (1968) 209-15.
[5] Bretherton, FP. The motion of rigid particles in a shear flow at low Reynolds number, Journal of Fluid Mechanics. 14 (1962) 284-304.
[6] Jeffery, GB, Filon, LNG. The motion of ellipsoidal particles immersed in a viscous fluid. 102 (1922) 161-79.
[7] Forgacs, OL, Mason, SG. Particle motions in sheared suspensions: X. Orbits of flexible threadlike particles, Journal of Colloid Science. 14 (1959) 473-91.
[8] Forgacs, OL, Robertson, AA, Mason, SG. The hydrodynamic behaviour of paper-making fibres, Pulp Paper Mag Can. 59 (1958) 117-28.
[9] Yamamoto, S, Matsuoka, T. A method for dynamic simulation of rigid and flexible fibers in a flow field, The Journal of Chemical Physics. 98 (1993) 644-50.
[10] Yamamoto, S, Matsuoka, T. Dynamic simulation of fiber suspensions in shear flow, The Journal of Chemical Physics. 102 (1995) 2254-60.
[11] Ross, RF, Klingenberg, DJ. Dynamic simulation of flexible fibers composed of linked rigid bodies. 106 (1997) 2949-60.
[12] Nyland, GH, Skjetne, P, Mikkelsen, A, Elgsaeter, A. Brownian dynamics simulation of needle chains. 105 (1996) 1198-207.
[13] Skjetne, P. Implementation and performance of the needle chain-algorithm for Brownian dynamics simulation1999.
[14] Schmid, CF, Switzer, LH, Klingenberg, DJ. Simulations of fiber flocculation: Effects of fiber properties and interfiber friction. 44 (2000) 781-809.
[15] Wang, G, Yu, W, Zhou, C. Optimization of the rod chain model to simulate the motions of a long flexible fiber in simple shear flows, European Journal of Mechanics - B/Fluids. 25 (2006) 337-47.
[16] Goldstein, RE, Powers, TR, Wiggins, CH. The Viscous Nonlinear Dynamics of Twist and Writhe, Physical Review Letters. 80 (1998) 5232-5.
[17] Becker, L, Shelley, M. Instability of Elastic Filaments in Shear Flow Yields First-Normal-Stress Differences, Physical review letters. 87 (2001) 198301.
[18] Johnson, RE. An improved slender-body theory for Stokes flow, Journal of Fluid Mechanics. 99 (1980) 411-31.
[19] Keller, JB, Rubinow, SI. Slender-body theory for slow viscous flow, Journal of Fluid Mechanics. 75 (1976) 705-14.
[20] Shelley, MJ, Ueda, T. The Stokesian hydrodynamics of flexing, stretching filaments, Physica D: Nonlinear Phenomena. 146 (2000) 221-45.
[21] Tornberg, A-K, Gustavsson, K. A numerical method for simulations of rigid fiber suspensions, Journal of Computational Physics. 215 (2006) 172-96.
[22] Tornberg, A-K, Shelley, MJ. Simulating the dynamics and interactions of flexible fibers in Stokes flows, Journal of Computational Physics. 196 (2004) 8-40.
[23] Peskin, CS. Numerical analysis of blood flow in the heart, Journal of Computational Physics. 25 (1977) 220-52.
[24] Peskin, CS. The Fluid Dynamics of Heart Valves: Experimental, Theoretical, and Computational Methods, Annual Review of Fluid Mechanics. 14 (1982) 235-59.
[25] Peskin , C. Peskin, C.S.: The immersed boundary method. Acta Numerica 11, 479-517, Acta Numerica. 11 (2002) 479-517.
[26] Stockie, JM, Green, SI. Simulating the Motion of Flexible Pulp Fibres Using the Immersed Boundary Method,

Journal of Computational Physics. 147 (1998) 147-65.
[27] Zhu, L, Peskin, CS. Simulation of a Flapping Flexible Filament in a Flowing Soap Film by the Immersed Boundary Method, Journal of Computational Physics. 179 (2002) 452-68.
[28] Huang, W-X, Shin, SJ, Sung, HJ. Simulation of flexible filaments in a uniform flow by the immersed boundary method, Journal of Computational Physics. 226 (2007) 2206-28.
[29] Tian, F-B, Luo, H, Zhu, L, Liao, JC, Lu, X-Y. An efficient immersed boundary-lattice Boltzmann method for the hydrodynamic interaction of elastic filaments, Journal of Computational Physics. 230 (2011) 7266-83.
[30] Yuan, H-Z, Niu, X-D, Shu, S, Li, M, Yamaguchi, H. A momentum exchange-based immersed boundary-lattice Boltzmann method for simulating a flexible filament in an incompressible flow, Computers & Mathematics with Applications. 67 (2014) 1039-56.
[31] Goza, A, Colonius, T. A strongly-coupled immersed-boundary formulation for thin elastic structures, Journal of Computational Physics. 336 (2017) 401-11.
[32] Cui, J, Lin, Z, Jin, Y, Liu, Y. Numerical simulation of fiber conveyance in a confined channel by the immersed boundary-lattice Boltzmann method, European Journal of Mechanics - B/Fluids. 76 (2019) 422-33.
[33] Zhu, L. Simulation of an inhomogeneous elastic filament falling in a flowing viscous fluid, Physics of Fluids. 19 (2007) 017113.
[34] Zhu, L, Chin, RCY. Simulation of elastic filaments interacting with a viscous pulsatile flow, Computer Methods in Applied Mechanics and Engineering. 197 (2008) 2265-74.
[35] Kanchan, M, Maniyeri, R. Numerical analysis of the buckling and recuperation dynamics of flexible filament using an immersed boundary framework, International Journal of Heat and Fluid Flow. 77 (2019) 256-77.
[36] Pei, Z, Yu, C. Numerical study on the effect of nozzle pressure and yarn delivery speed on the fiber motion in the nozzle of Murata vortex spinning, Journal of Fluids and Structures. 27 (2011) 121-33.
[37] Connell, BSH, Yue, DKP. Flapping dynamics of a flag in a uniform stream, Journal of Fluid Mechanics. 581 (2007) 33-67.
[38] Alben, S. Simulating the dynamics of flexible bodies and vortex sheets, Journal of Computational Physics. 228 (2009) 2587-603.
[39] Liu, Q-Y, Tang, X-Y, Chen, D-D, Xu, Y-q, Tian, F-B. Hydrodynamic study of sperm swimming near a wall based on the immersed boundary-lattice Boltzmann method, Engineering Applications of Computational Fluid Mechanics. 14 (2020) 853-70.
[40] Klar, A, Marheineke, N, Wegener, R. Hierarchy of mathematical models for production processes of technical textiles. 89 (2009) 941-61.
[41] Luo, L-S, Liao, W, Chen, X, Peng, Y, Zhang, W. Numerics of the lattice Boltzmann method: Effects of collision models on the lattice Boltzmann simulations, Physical review E, Statistical, nonlinear, and soft matter physics. 83 (2011) 056710.
[42] Sotiropoulos, F, Yang, X. Immersed boundary methods for simulating fluid–structure interaction, Progress in Aerospace Sciences. 65 (2014) 1-21.
[43] Niu, XD, Shu, C, Chew, YT, Peng, Y. A momentum exchange-based immersed boundary-lattice Boltzmann method for simulating incompressible viscous flows, Physics Letters A. 354 (2006) 173-82.
[44] Xu, S, Wang, ZJ. An immersed interface method for simulating the interaction of a fluid with moving boundaries, Journal of Computational Physics. 216 (2006) 454-93.
[45] Russell, D, Jane Wang, Z. A cartesian grid method for modeling multiple moving objects in 2D incompressible viscous flow, Journal of Computational Physics. 191 (2003) 177-205.
[46] Zhang, J, Childress, S, Libchaber, A, Shelley, M. Flexible filaments in a flowing soap film as a model for one-dimensional flags in a two-dimensional wind, Nature. 408 (2000) 835-9.

[47] Farutin, A, Piasecki, T, Słowicka, AM, Misbah, C, Wajnryb, E, Ekiel-Jeżewska, ML. Dynamics of flexible fibers and vesicles in Poiseuille flow at low Reynolds number, Soft matter. 12 (2016) 7307-23.
[48] Słowicka, AM, Ekiel-Jeżewska, ML, Sadlej, K, Wajnryb, E. Dynamics of fibers in a wide microchannel, The Journal of Chemical Physics. 136 (2012) 044904.